Loss of TET reprograms Wnt signaling through impaired demethylation to promote lung cancer development

Qin Xu[a,1], Chao Wang[a,1], Jia-Xin Zhou[a], Zhi-Mei Xu[a], Juan Gao[a], Pengfei Sui[b], Colum P. Walsh[c,d], Hongbin Ji[b,e,f,2], and Guo-Liang Xu[a,g,2]

[a]State Key Laboratory of Molecular Biology, Shanghai Institute of Biochemistry and Cell Biology, Center for Excellence in Molecular Cell Science, Chinese Academy of Sciences, University of Chinese Academy of Sciences, Shanghai 200031, China; [b]State Key Laboratory of Cell Biology, Shanghai Institute of Biochemistry and Cell Biology, Center for Excellence in Molecular Cell Science, Chinese Academy of Sciences, University of Chinese Academy of Sciences, Shanghai 200031, China; [c]Genomic Medicine Research Group, Biomedical Sciences, Ulster University, Coleraine BT52 1SA, United Kingdom; [d]Centre for Research & Development, Region Gävleborg/Uppsala University, Gävle 801 88, Sweden; [e]School of Life Science and Technology, ShanghaiTech University, Shanghai 201210, China; [f]School of Life Science, Hangzhou Institute for Advanced Study, University of Chinese Academy of Sciences, Hangzhou 310024, China; and [g]Shanghai Key Laboratory of Medical Epigenetics, Institutes of Biomedical Sciences, Shanghai Medical College of Fudan University, Chinese Academy of Medical Sciences (RU069), Shanghai 200032, China

Edited by Jonathan Kurie, Thoracic/Head and Neck Medical Oncology, The University of Texas MD Anderson Cancer Center, Houston, TX; received April 22, 2021; accepted November 17, 2021 by Editorial Board Member Anton Berns

Oncogenic imbalance of DNA methylation is well recognized in cancer development. The ten-eleven translocation (TET) family of dioxygenases, which facilitates DNA demethylation, is frequently dysregulated in cancers. How such dysregulation contributes to tumorigenesis remains poorly understood, especially in solid tumors which present infrequent mutational incidence of *TET* genes. Here, we identify loss-of-function mutations of *TET* in 7.4% of human lung adenocarcinoma (LUAD), which frequently co-occur with oncogenic *KRAS* mutations, and this co-occurrence is predictive of poor survival in LUAD patients. Using an autochthonous mouse model of $Kras^{G12D}$-driven LUAD, we show that individual or combinational loss of *Tet* genes markedly promotes tumor development. In this *Kras*-mutant and *Tet*-deficient model, the premalignant lung epithelium undergoes neoplastic reprogramming of DNA methylation and transcription, with a particular impact on Wnt signaling. Among the Wnt-associated components that undergo reprogramming, multiple canonical Wnt antagonizing genes present impaired expression arising from elevated DNA methylation, triggering aberrant activation of Wnt signaling. These impairments can be largely reversed upon the restoration of TET activity. Correspondingly, genetic depletion of β-*catenin*, the transcriptional effector of Wnt signaling, substantially reverts the malignant progression of *Tet*-deficient LUAD. These findings reveal TET enzymes as critical epigenetic barriers against lung tumorigenesis and highlight the therapeutic vulnerability of *TET*-mutant lung cancer through targeting Wnt signaling.

epigenetic barriers | DNA dioxygenases | lung adenocarcinoma | mouse models | Wnt antagonizing genes

Lung cancer is a lethal disease that accounts as a leading cause of cancer-related mortality worldwide, with an estimated 1.6 million deaths yearly (1). Lung adenocarcinoma (LUAD) represents the most common histological subtype of non–small-cell lung cancer (2). The most commonly mutated genes harbored in LUAD include protooncogenes *KRAS* and *EGFR* and tumor suppressor genes *TP53*, *KEAP1*, and *STK11* (3–5). Identification of targetable driver gene alterations during cancer evolution has revolutionized the management of oncogene-addicted cancers with tumor-specific genotyping (6–9). Introduction of immunotherapy has also signaled a new direction for the treatment of advanced stage lung cancer (10, 11). However, clinical benefits from these therapies remain poor, and notable improvements are typically short lived (12). Therefore, there is an unmet need for better mechanistic understanding of lung tumorigenesis, which could be leveraged for development of more effective and durable therapeutic modalities to improve clinical management.

Aside from extensive studies of the genetic landscape underlying tumor pathogenesis, tumor cells are also known to be epigenetically altered (13–15). Epigenetic dysregulations often emerge from disruption of DNA and histone modifying enzymes (16, 17). Oncogenic alterations in DNA methylation are well documented (18), which include global hypomethylation of the genome and localized hypermethylation at specific gene promoters (19). DNA hypermethylation on promoter CpG islands of tumor suppressor genes frequently silences their expression and thus contributes to oncogenesis. Counter to DNA methylation, the process of demethylation remained elusive until proteins of TET family (TET1, TET2, and TET3) were identified as 5-methylcytosine dioxygenases (20). TET

Significance

Previous studies have identified the tumor-suppressive function of TET enzymes in hematological cancers. Given the differential mutational incidence and lacking functional validation, how TET contributes to carcinogenesis in solid tumors remains largely undefined. Here, we report that *TET* mutations co-occur with *KRAS* mutations, and such co-occurrence predicts poor survival in human LUAD. Using genetically engineered mouse models (GEMMs), we show that inactivation of *TET* cooperates with oncogenic *KRAS* to potentiate LUAD development, and that this effect is preferentially induced by augmented Wnt signaling as a consequence of impaired expression of Wnt-associated antagonists due to DNA hypermethylation. Our work reveals the tissue-specific and context-dependent roles of TET during carcinogenesis and implicates Wnt signaling as a therapeutic modality for *TET*-mutant lung tumors.

Author contributions: Q.X., H.J., and G.-L.X. designed research; Q.X., C.W., J.-X.Z., Z.-M.X., and J.G. performed research; H.J. contributed new reagents/analytic tools; Q.X., C.W., J.-X.Z., J.G., P.S., and C.P.W. analyzed data; and Q.X., H.J., and G.-L.X. wrote the paper.

The authors declare no competing interest.

This article is a PNAS Direct Submission. J.K. is a guest editor invited by the Editorial Board.

[1]Q.X. and C.W. contributed equally to this work.

[2]To whom correspondence may be addressed. Email: hbji@sibcb.ac.cn or glxu@sibcb.ac.cn.

This article contains supporting information online at http://www.pnas.org/lookup/suppl/doi:10.1073/pnas.2107599119/-/DCSupplemental.

Published February 2, 2022.

proteins successively oxidize 5-methylcytosine (5mC) to 5-hydroxymethylcytosine (5hmC), 5-formylcytosine (5fC), and 5-carboxylcytosine (5caC) (21, 22). Subsequently, 5fC and 5caC, the higher-oxidation products, can be excised by DNA glycosylase TDG and then replaced with an unmodified cytosine via base excision repair (22), thereby achieving active demethylation (23, 24). *TET* family genes, especially *TET2*, are found to be frequently mutated in a variety of hematological malignancies (25–28). In the hematopoietic setting, loss-of-function *TET* genes drive malignant transformation (29–33). In comparison, due to a lack of relevant disease models (34–36), whether *TET* deficiency has a similar effect in solid cancers has not been fully investigated. Given that tumors are genetically heterogeneous and often bear varying types of somatic alterations, it remains to be determined if and how mutating *TET* genes would confer a selective advantage in the onset and progression of solid tumors.

In this study, we identified mutations of *TET* genes in 7.4% of human LUAD, which frequently coincide with oncogenic *KRAS* mutations. By using $Kras^{G12D}$-driven autochthonous genetically engineered mouse models (GEMMs), we interrogated the pathological role of TET dioxygenases in lung cancer development. Our results showed that inactivation of *TET* cooperated with $Kras^{G12D}$ to accelerate mouse LUAD development, and this could be largely alleviated by the reintroduction of TET catalytic activity. We further found that TET loss led to augmented Wnt signaling through down-regulating gene expression of Wnt-related antagonists (such as *Lrp4* and *Ctnnbip1*) via DNA hypermethylation and genetic inhibition of Wnt pathway potently alleviated *Tet*-deficient LUAD progression. These findings clearly elucidate the tumor-suppressive function of TET enzymes in *Kras*-driven LUAD development and implicate Wnt signaling as a potential therapeutic target for patients with *TET*-deficient lung cancer.

Results

Loss-of-Function *TET* Mutations Co-occur with *KRAS* Mutations in Human LUAD. To address the involvement of TET in lung cancer, we first examined the genomic alterations of *TET* genes in human LUAD using The Cancer Genome Atlas (TCGA) datasets together with other datasets (37–40). Of all types of genomic alterations of *TET* genes, mutations were predominant (*SI Appendix*, Fig. S1*A*), with a frequency of 7.4% in all LUAD patients, among which *TET1*, *TET2*, and *TET3* mutations account for 4, 1.6, and 1.8%, respectively (*SI Appendix*, Fig. S1*B*). The vast majority of these mutations were missense mutations, and the remaining ~17.3% were truncating mutations (*SI Appendix*, Fig. S1 *C* and *D*). These numbers are similar to previous reports of *TET* mutations in other solid cancers such as clear-cell renal cell carcinoma (41) and colon (42) and prostate cancers (43). As one of the most common oncogenic drivers, *KRAS* is mutated in up to 30% of human LUAD (*SI Appendix*, Fig. S1*B*). Interestingly, we identified a significant co-occurrence between *TET* and *KRAS* mutations (*SI Appendix*, Fig. S1*E*). About 32% of *TET*-mutated LUAD carried *KRAS* mutations, and about 7% of *KRAS*-mutated LUAD harbored mutations in *TET* family members (*SI Appendix*, Fig. S1*E*). Moreover, compared to either *KRAS* or *TET* mutations alone, their concurrence, particularly the combination of *KRAS* with *TET2* or *TET3*, was clearly associated with reduced survival of LUAD patients (*SI Appendix*, Fig. S1*F*). In contrast, mutations in *EGFR*, another well-known oncogenic driver, were mutually exclusive with *TET* mutations (*SI Appendix*, Fig. S2 *A* and *B*), and there was no evident correlation of survival in LUAD patients with either *EGFR* or *TET* mutations alone or both (*SI Appendix*, Fig. S2*C*).

We further characterized the impacts of *TET* mutations on their own gene expression and catalytic activity. In the TCGA LUAD datasets, we found that *TET* mutations were accompanied with lower expression of *TET* mRNA, regardless of *KRAS* status (*SI Appendix*, Fig. S3 *A* and *B*). Consistently, we observed a higher level of DNA methylation in *TET*-mutant human LUAD (*SI Appendix*, Fig. S3*C*). Next, we focused on *TET* missense mutations to test catalytic activity because of their relatively high frequency in human LUAD (*SI Appendix*, Fig. S1*D*). Among the six human LUAD-derived *TET2* missense mutations examined, five mutations showed decreased dioxygenase activity in an assay using ectopic expression of the full-length mutants in HEK293T cells (*SI Appendix*, Fig. S3 *D* and *E*).

In addition, we observed decreased *TET* expression in TCGA LUAD samples compared with healthy tissues, particularly *TET2* and *TET3* (*SI Appendix*, Fig. S3*F*). Lower expression of *TET* mRNA was also associated with poorly differentiated status in *TET* wild-type human LUAD (*SI Appendix*, Fig. S3*G*). Correspondingly, low *TET* expression was associated with worse patient survival (*SI Appendix*, Fig. S3 *H* and *I*). Collectively, these observations suggest a putative tumor-suppressive role of *TET* genes in human LUAD, particularly in LUAD harboring *KRAS* mutations.

***Tet* Triple Knockout Synergizes with $Kras^{G12D}$ to Accelerate LUAD.** To evaluate the functional importance of TET in LUAD development, *Tet* conditional knockout mice ($Tet1^{flox/flox}$; $Tet2^{flox/flox}$; $Tet3^{flox/flox}$) (44) and *Kras*-driven autochthonous GEMM (45) were used to obtain the three cohorts: $Kras^{LSL\text{-}G12D/+}$ (hereafter K), $Kras^{LSL\text{-}G12D/+}$; $Tet1^{flox/+}$; $Tet2^{flox/+}$; $Tet3^{flox/+}$ (hereafter KT Het), and $Kras^{LSL\text{-}G12D/+}$; $Tet1^{flox/flox}$; $Tet2^{flox/flox}$; $Tet3^{flox/flox}$ (hereafter KT) (*SI Appendix*, Fig. S4 *A* and *B*). In these models, intranasal infection of K, KT Het, and KT mice with a Cre-expressing adenovirus under the control of CMV promoter (Ad-CMV-Cre) allows the simultaneous induction of the deletion of *Tet* genes and the expression of oncogenic $Kras^{G12D}$ in lung epithelial cells to initiate lung tumorigenesis (46) (*SI Appendix*, Fig. S4*C*).

Strikingly, inactivation of all three *Tet* genes strongly potentiated $Kras^{G12D}$-driven LUAD development. Compared to K controls, KT mice exhibited substantially accelerated tumor growth with enhanced tumor burden (Fig. 1 *A* and *B*), and showed increased tumor lesions with a higher percentage progressing to advanced adenocarcinoma at 12 wk post–adenoviral infection (Fig. 1 *C* and *D* and *SI Appendix*, Fig. S5*A*). The markedly shortened survival of KT mice underscored the lethal effect of *Tet* deficiency (Fig. 1*E*). Notably, elevated tumorigenic potential was also observed in KT Het mice (Fig. 1 *A*–*E*), suggesting that haploinsufficiency of *Tet* genes could also promote the formation of *Kras*-driven LUAD. During tumor progression from 8 to 12 wk postinfection, a higher rate of cell proliferation in KT tumors was observed by Ki-67 immunohistochemistry (*SI Appendix*, Fig. S5 *B* and *C*), accounting for rapidly elevated tumor burden (*SI Appendix*, Fig. S5 *D* and *E*). However, in the absence of oncogenic $Kras^{G12D}$, even if inactivating all three *Tet* genes, the morphology and lineage of lung epithelium appear normal even at 54 wk post–adenoviral infection (*SI Appendix*, Fig. S5 *F* and *G*), implying that *Tet* deficiency alone is insufficient to drive the formation of neoplastic lesions.

To characterize the differentiation state of *Tet*-deficient lung tumors, we stained serial sections for lung epithelial lineage-specific markers, including lung transcription factor NKX2-1 (NK2 homeobox 1), alveolar type 2 (AT2) cell marker SPC (surfactant protein C), and club cell marker SCGB1A1 (secretoglobin family 1A member 1). Similar to K tumors, KT tumors were frequently positive for NKX2-1 and SPC and negative for SCGB1A1 (Fig. 1*F*), reflecting an AT2 origin of LUAD (47–50). However, a large number of KT tumors had areas with low or completely absent expression of NKX2-1 and SPC (Fig.

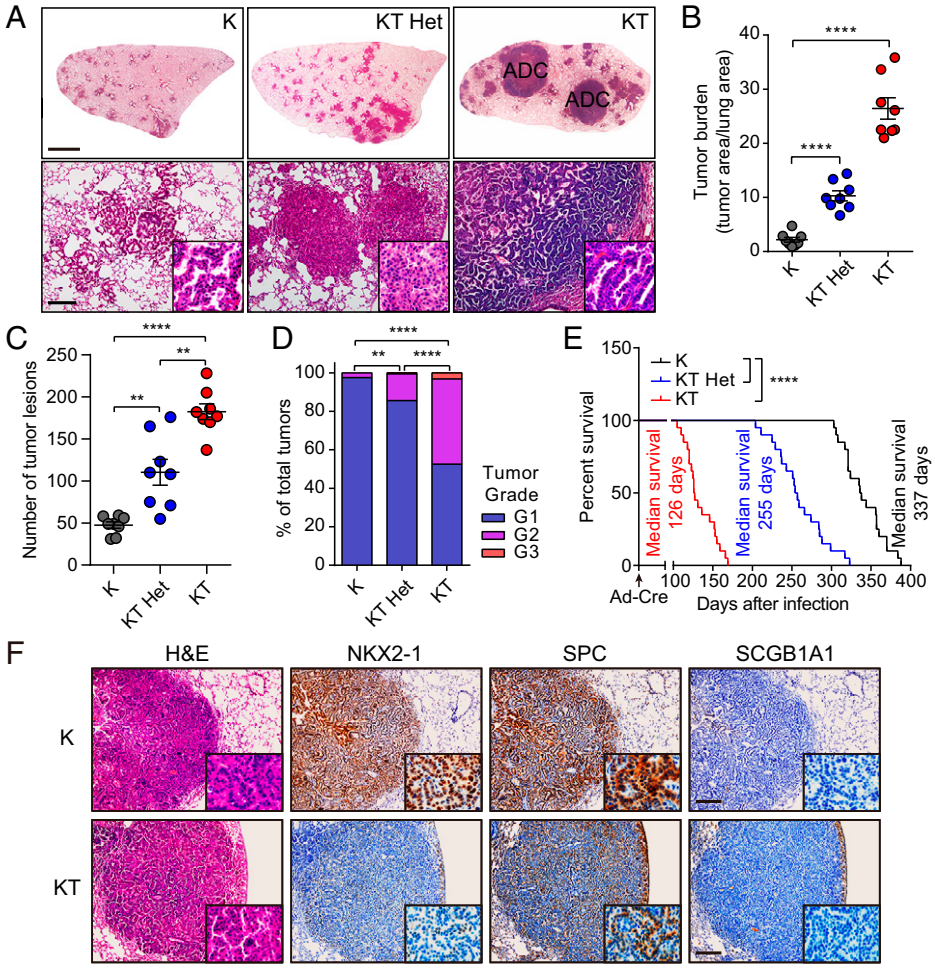

Fig. 1. Inactivation of *Tet* family genes potentiates the development of *Kras*-driven LUAD in mice. (*A*) Representative H&E-stained lung sections. Lung tissues were collected from K, KT Het, and KT mice at 12 wk after Ad-CMV-Cre intranasal inhalation. *Insets* are magnified 4×. (Scale bars, 2 mm [*Top*] and 200 μm [*Bottom*].) Corresponding quantification of (*B*) tumor burden (total tumor area/total lung area), (*C*) tumor number, and (*D*) tumor grade in mice of indicated genotypes. Each circle represents an individual mouse. $n = 8$ mice for each genotype. G1, grade 1 atypical adenomatous hyperplasia; G2, grade 2 adenoma; G3, grade 3 adenocarcinoma (ADC). In *C*, for K, $n = 380$ lesions; for KT Het, $n = 833$ lesions; and for KT, $n = 1{,}459$ lesions. (*E*) Kaplan–Meier survival analysis for mice of indicated genotypes. $n = 20$ mice for each group. Data are presented as mean ± SEM. Statistical significance was assessed using two-tailed unpaired Student's *t* test with Welch's correction (*B* and *C*) or χ^2 test (*D*) or log-rank (Mantel–Cox) test (*E*). $^{**}P \leq 0.01$; $^{****}P \leq 0.0001$. (*F*) Immunohistochemistry (IHC) images for NKX2-1, SPC, and SCGB1A1 staining in K tumors at 24 wk after Ad-CMV-Cre infection and in KT tumors at 12 wk after Ad-CMV-Cre infection. (*Left*) H&E staining. *Insets* are magnified 10×. (Scale bars, 200 μm.)

1*F*), suggesting that *Tet* loss may result in more malignant lesions associated with poorly differentiated state. Together, these results establish *Tet* genes as critical tumor suppressors in *Kras*-driven mouse LUAD development.

***Tet2* and *Tet3* Act as Key Suppressors against LUAD Development.** To elucidate the contribution of individual *Tet* genes to the control of LUAD development, we generated additional GEMMs of *Tet* single knockout including $Kras^{LSL\text{-}G12D/+}$; $Tet1^{flox/flox}$, $Kras^{LSL\text{-}G12D/+}$; $Tet2^{flox/flox}$, and $Kras^{LSL\text{-}G12D/+}$; $Tet3^{flox/flox}$ (hereafter KT1, KT2, and KT3, respectively) (*SI Appendix*, Fig. S4 *A* and *B*). In contrast to K controls, KT1, KT2, or KT3 mice all showed greatly enhanced tumor burden (Fig. 2 *A* and *B*), more lesions progressing to higher tumor grades at 12 wk post–adenoviral infection (Fig. 2 *C* and *D*), and impaired survival with varying degrees (Fig. 2 *E*). Among the single mutants, KT2 mice were the most severe in tumor formation (Fig. 2 *A*–*D*). Given that *Tet2* and *Tet3* transcripts were more abundant than *Tet1* in normal lung tissues (*SI Appendix*, Fig. S6*A*) and in K tumors compared to those in matched tumor-free tissues (*SI Appendix*, Fig. S6*B*), we then generated double knockout GEMM KT23 ($Kras^{LSL\text{-}G12D/+}$; $Tet2^{flox/flox}$; $Tet3^{flox/flox}$) (*SI Appendix*, Fig. S4 *A* and *B*) to test if *Tet2* and *Tet3* can function together to suppress LUAD development. As expected, double knockout of *Tet2* and *Tet3* led to stronger tumorigenic phenotypes than any of the single mutants, almost comparable to the complete knockout of all three *Tet* genes (Fig. 2 *A*–*E*). Moreover, highly malignant lesions triggered by single or double knockout of *Tet* genes exhibited lower expression of NKX2-1 and SPC (*SI Appendix*, Fig. S6 *C*–*F*), indicative of their poorly differentiated state. Together, these data provide evidence for the tumor-suppressive role of individual *Tet* genes, especially *Tet2* and *Tet3*, in antagonizing LUAD development.

TET Catalytic Activity Is Required for Antagonizing LUAD Development. To determine whether the activity of 5mC oxidation is directly involved in the control of lung tumorigenesis, we first attempted to obtain mouse primary LUAD cells using Cre-mediated $Rosa26^{LSL\text{-}tdTomato/+}$ reporter mice (51), which were crossed into K or KT mice to enable direct isolation of tdTomato$^+$ cancer cells by fluorescence-activated cell sorting (FACS) (*SI Appendix*, Fig. S7*A*). As mutant *Kras* alone is

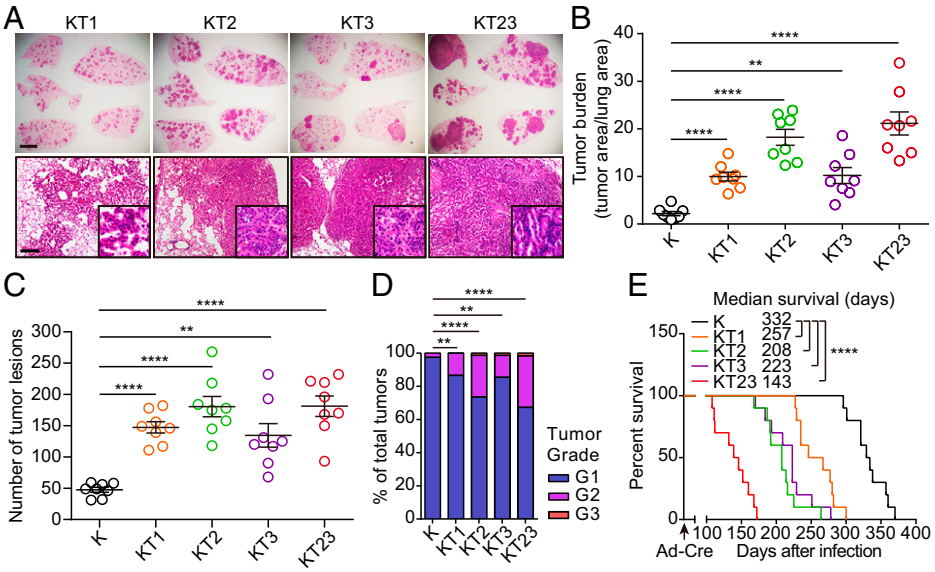

Fig. 2. *Tet* genes suppress mouse LUAD development in a dosage-dependent manner. (*A*) Representative images of H&E-stained tumor-bearing lung sections from KT1, KT2, KT3, and KT23 mice at 12 wk after Ad-CMV-Cre intranasal inhalation. *Insets* are magnified 4×. (Scale bars, 2 mm [*Top*] and 200 μm [*Bottom*].) Corresponding quantification of (*B*) tumor burden, (*C*) tumor number, and (*D*) tumor grade in mice of indicated genotypes. Each circle represents an individual mouse. $n = 8$ mice for each genotype. For KT1, $n = 1{,}178$ lesions; for KT2, $n = 1{,}444$ lesions; for KT3, $n = 1{,}076$ lesions; and for KT23, $n = 1{,}449$ lesions. (*E*) Kaplan–Meier survival curves for mice of indicated genotypes. $n = 10$ mice for each group. Data are presented as mean ± SEM. Statistical significance was calculated using two-tailed unpaired Student's *t* test with Welch's correction (*B* and *C*) or χ^2 test (*D*) or log-rank (Mantel–Cox) test (*E*). $^{**}P \leq 0.01$; $^{****}P \leq 0.0001$.

weakly oncogenic and K tumor cells are difficult to culture in vitro (52), KT but not K cell lines were successfully established (*SI Appendix*, Fig. S7 *B* and *C*). We then validated tumor formation capacity of the established KT cell lines by subcutaneous allograft assay (*SI Appendix*, Fig. S7*D*). Next, we ectopically expressed a Tet2 construct containing the core catalytic domain (hereafter Tet2CD) or the catalytically-inactive counterpart with disrupted iron-binding site ($H_{1295}R_{1296}D_{1297}$ mutated to $Y_{1295}R_{1296}A_{1297}$) (hereafter Tet2HD) in KT cells (*SI Appendix*, Fig. S7 *E–G*). As a result, expression of Tet2CD, but not Tet2HD, resulted in 5hmC regeneration, concomitant with 5mC reduction in KT cells (*SI Appendix*, Fig. S7 *H* and *I*). Expression of the catalytically-active Tet2CD in KT cells also attenuated cell proliferation and subcutaneous allograft formation (*SI Appendix*, Fig. S7 *J* and *K*). Similarly, reintroducing the full-length wild-type Tet2, but not the catalytically-inactive mutant, decreased proliferation in KT cells (*SI Appendix*, Fig. S7 *L–O*). These data suggest a dependence of the TET enzymatic activity for its anti-LUAD function.

To validate the requirement of dioxygenase activity for the control of LUAD development in vivo, we generated lentiviruses expressing both Cre recombinase and Tet2CD or Tet2HD for administration into KT mice (Fig. 3*A*). To test the lentiviral constructs in vitro, we employed an engineered 3T3 reporter cell line, which expresses GFP following the exposure to Cre (*SI Appendix*, Fig. S8*A*). The lentiviruses that we generated were functionally validated by qRT-PCR, Western blot, and dot blot (*SI Appendix*, Fig. S8 *B–F*) and then delivered through intranasal administration into KT mice (Fig. 3*A*). Consistent with our findings in vitro, the expression of Tet2CD, but not catalytically-inactive Tet2HD, reversed multiple tumorigenic phenotypes caused by *Tet* deficiency, leading to diminished tumor burden (Fig. 3 *B* and *C*), decreased tumor numbers, and impaired tumor progression to high-grade lesions (Fig. 3 *D* and *E*). As expected, stronger 5hmC signal appeared in KT tumors treated with Cre-Tet2CD lentivirus (Fig. 3*F*). Thus, these results demonstrate that dioxygenase activity is required for suppressing LUAD development.

TET Loss Causes Wnt-Associated Transcriptional and Methylation Alterations in Premalignancy. We next sought to understand how deficiency in TET activity contributes to lung tumorigenesis. To identify the molecular alterations induced by *Tet* loss in early-stage neoplasia in vivo, genetic lineage-labeling K and KT GEMMs with *Rosa26*$^{LSL\text{-}tdTomato/+}$ reporter allele were used for the isolation of premalignant lung epithelial cells (Fig. 4*A*). Through a $DAPI^-/tdTomato^+/EPCAM^+/CD45^-/CD31^-$ gating strategy (*SI Appendix*, Fig. S9*A*), $tdTomato^+$ lung epithelial cells (hereafter referred to as premalignant cells) were sorted individually from K or KT mice at 3 wk post–Ad-CMV-Cre infection. At this early stage, the fraction of premalignant cell population from KT mice (0.28 to 0.93%) was comparable to that from K control mice (0.26 to 1.24%) (*SI Appendix*, Fig. S9 *B* and *C*).

To profile transcriptional changes which occurred early on after the induced oncogenic transformation, we performed RNA sequencing (RNA-seq) on ∼500 isolated premalignant cells. The gene expression of lung epithelial markers was examined to verify the epithelial source of the isolated cells, and the expression levels of these marker genes were similar between K and KT cells (*SI Appendix*, Fig. S9*D*). Intriguingly, after 3 wk post–adenoviral infection, the transcriptome of KT premalignant cells was already distinct from that of K control cells using a principal component analysis (PCA) (Fig. 4*B*). Differentially expression analysis identified 705 genes that were significantly altered, with 579 up-regulated and 126 down-regulated in KT premalignant cells (Fig. 4*C*). Among the most differentially expressed genes (DEGs), gene ontology (GO) analysis identified an expression signature in KT premalignant cells featuring the up-regulated Wnt signaling pathway (Fig. 4 *D* and *E*). Additionally, whole-genome bisulfite sequencing (WGBS) by postbisulfite adaptor tagging (PBAT) was also performed to assess the alterations on DNA methylation in KT premalignant cells. We found that the overall CpG methylation level increased slightly across the whole genome in KT premalignant cells compared to K control cells (60.95% vs. 58.56%) (*SI Appendix*, Fig. S9*E*). Localized increase in CpG methylation

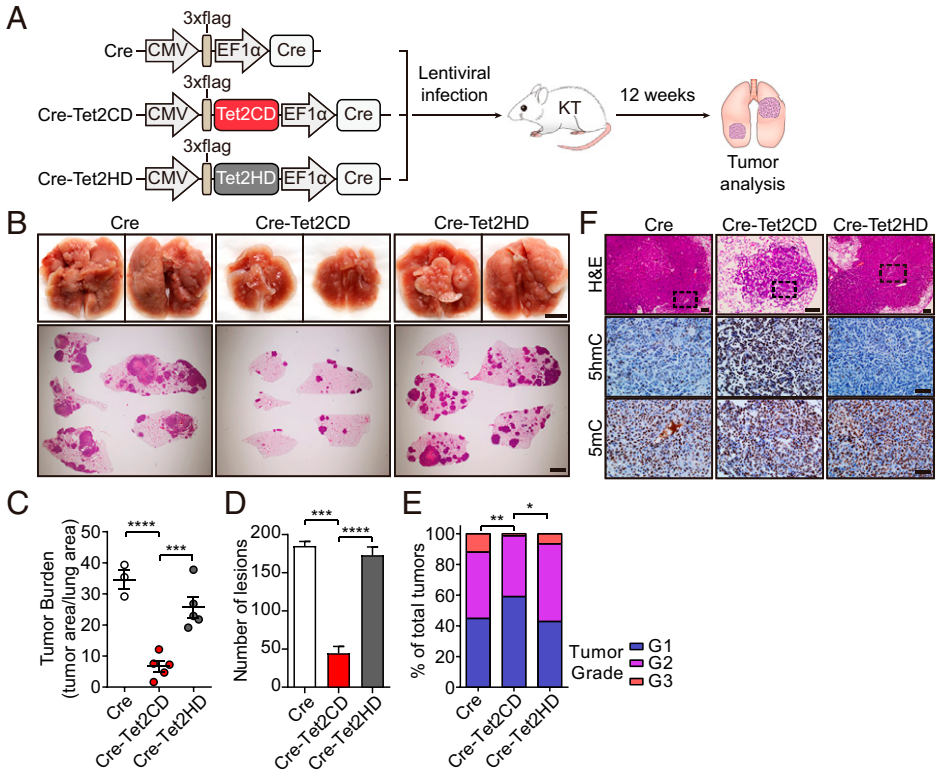

Fig. 3. Restoration of catalytically-active TET potently mitigates enhanced LUAD development in KT mice. (*A*) Schematic of lung tumorigenesis in KT mice administered with lentiviruses of Cre, Cre-Tet2CD (wild type), or Cre-Tet2HD (mutant). The lentiviral constructs are shown. At 12 wk after intranasal inhalation, lung tissues were collected for histopathological analysis. (*B*) Representative whole-mount views of tumor-bearing lung tissues and H&E-stained lung tumor sections from KT mice administered with indicated lentiviruses. Corresponding quantification of (*C*) tumor burden, (*D*) tumor number, and (*E*) tumor grade in KT mice with indicated lentiviral treatments. For tumor burden measurement, $n = 3$ mice infected with Cre lentivirus, and $n = 5$ mice infected with Cre-Tet2CD or Cre-Tet2HD lentivirus, respectively. For lesion number and tumor grade quantification, 370 lesions were counted from two mice infected with Cre lentivirus, 178 lesions from four mice infected with Cre-Tet2CD lentivirus, and 692 lesions from four mice infected with Cre-Tet2HD lentivirus. Data are presented as mean ± SEM. Statistical significance was assessed using two-tailed unpaired Student's *t* test (*C* and *D*) or χ^2 test (*E*). $^*P \le 0.05$; $^{**}P \le 0.01$; $^{***}P \le 0.001$; $^{****}P \le 0.0001$. (*F*) H&E and immunohistochemistry (IHC) images for 5hmC and 5mC staining in KT tumors with indicated lentiviruses. Dashed rectangles in H&E pictures mark corresponding magnified regions in adjacent slides shown in 5hmC and 5mC IHC staining. (Scale bars, 5 mm [*B*, *Top*]; 2 mm [*B*, *Bottom*]; 100 μm [*F*, *Top*]; and 50 μm [*F*, *Middle* and *Bottom*].)

was found across multiple types of genomic elements (*SI Appendix*, Fig. S9 *E* and *F*). Specifically, 6,578 hypermethylated differentially methylated regions (DMRs) and 3,445 hypomethylated DMRs were defined in KT premalignant cells (Fig. 4*F*), reflecting overall gain of methylation. Further genomic annotation revealed that the hypermethylated DMRs in KT premalignant cells were mostly enriched in gene bodies and followed by promoters and enhancers (Fig. 4*G*). Integration of transcriptional and methylation profiles identified the DEGs that exhibited hypermethylation at associated regulatory elements including the regions of gene body, promoter, and enhancer in KT premalignant cells. GO analysis of these hypermethylated DEGs revealed a significantly enriched fraction of Wnt-associated components (Fig. 4 *H* and *I*). These data suggest that early transcriptional augmentation of Wnt-associated components due to abnormal methylation caused by *TET* deficiency may contribute to the accelerated formation of early neoplastic lesions.

Reactivation of Wnt-Associated Antagonists Relies on TET-Mediated Demethylation in KT Cells. To ascertain the link between altered expression of Wnt-associated genes and impaired DNA methylation, we performed RNA-seq on established KT cell lines constitutively expressing Tet2CD or Tet2HD. PCA analysis revealed that transcriptional profiles of Tet2CD-expressing cells were clearly distinguishable from those of Tet2HD-expressing cells and their parental cells (*SI Appendix*, Fig. S10*A*). To identify transcriptional programs impacted by TET enzymatic activity, we obtained DEGs significantly altered in Tet2CD-expressing cells, when compared to the parental cells or Tet2HD-expressing cells, respectively (*SI Appendix*, Fig. S10 *B* and *C*). Among these overlapped DEGs, 253 were up-regulated, and 373 were down-regulated (*SI Appendix*, Fig. S10*D*). GO analysis of the up-regulated DEGs revealed a significant enrichment of genes associated with Wnt signaling, especially those antagonizing this pathway (e.g., *Lrp4*, *Ctnnbip1*, *Dact1*, *Tmem88*, and *Notum*) (Fig. 5*A* and *SI Appendix*, Fig. S10*E*). Consistent with these results, expression of the Wnt antagonizing genes was also up-regulated upon the reintroduction of the full-length Tet2 (Fig. 5*B*). The gene sets of down-regulated DEGs were most enriched for functions in cell proliferation and cell adhesion (*SI Appendix*, Fig. S10*F*). We next used TET-assisted pyridine borane sequencing (TAPS) (53) to compare the genome-wide methylome upon the restoration of dioxygenase activity in KT cells. A robust decline of CpG methylation occurred across the various genomic elements in Tet2CD-expressing KT cells (21.18%), compared to that in the parental (41.46%) or Tet2HD-expressing (35.90%) cells (*SI Appendix*, Fig. S11*A*). The majority of the identified DMRs were hypomethylated (*SI Appendix*, Fig. S11*B*), and these hypomethylated DMRs were mainly located in promoter regions (34.20%) (*SI Appendix*, Fig. S11*C*). Of note, among the 172 up-regulated DEGs with hypomethylated promoters in KT cells, genes of Wnt-associated

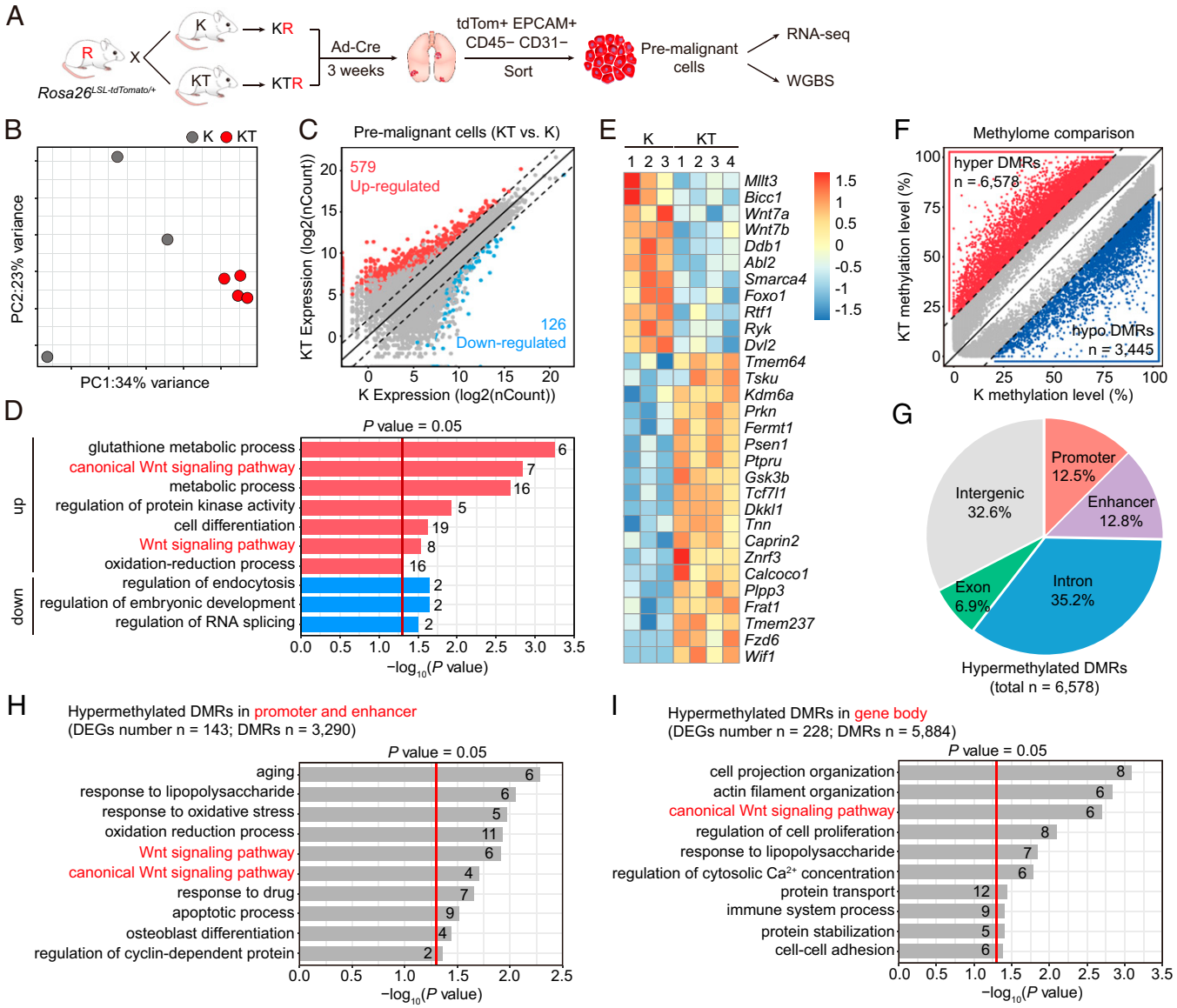

Fig. 4. TET loss induces the dysregulation of Wnt-associated transcription and methylation in premalignant lung epithelium. (*A*) Genetic lineage-labeling strategy to capture premalignant cells using *Rosa26* floxed-STOP-tdTomato reporter. *Rosa26*$^{LSL\text{-}tdTomato/+}$ (hereafter R), K, and KT mice were crossed to generate the following cohorts: *Kras*$^{LSL\text{-}G12D/+}$; *Rosa26*$^{LSL\text{-}tdTomato/+}$ (KR) and *Kras*$^{LSL\text{-}G12D/+}$; *Tet1* $^{flox/flox}$; *Tet2*$^{flox/flox}$; *Tet3* $^{flox/flox}$; *Rosa26*$^{LSL\text{-}tdTomato/+}$ (KTR). Mice were intranasally administered with Ad-CMV-Cre. After 3 wk, lungs were collected to sort DAPI$^-$/tdTomato$^+$/EPCAM$^+$/CD45$^-$/CD31$^-$ epithelial cells. (*B*) PCA of RNA-seq data from K and KT premalignant cells. Each dot represents an individual mouse. $n = 3$ for K mice; $n = 4$ for KT mice. (*C*) Scatter plot showing the DEGs in KT premalignant cells versus K cells. nCount represents the normalized counts (mean of the counts divided by size factors). The dashed lines indicate the fourfold change threshold for defining DEGs. Red and blue dots depict significantly changed genes [$\log_2$(fold change) ≥ 2 or ≤ -2 and adjusted *P* value ≤ 0.05], and gray dots depict genes without significant changes. (*D*) GO analysis of DEGs up-regulated or down-regulated in KT premalignant cells. The number of genes in each category is denoted. Wnt signaling pathway is indicated in red. DEGs here were those with $\log_2$(fold change) ≥ 2 or ≤ -2 and adjusted *P* value ≤ 0.01. (*E*) Heat map showing relative expression levels of Wnt-associated DEGs. DEGs here were those with $\log_2$(fold change) ≥ 1 or ≤ -1 and adjusted *P* value ≤ 0.05. (*F*) Global methylome comparison between K and KT premalignant cells using DMRs. DMRs were filtered by length (≤1,000 bp) and CpG number (at least five CpG sites). DMRs with at least 20% absolute methylation level difference between K and KT samples were defined as hypermethylated or hypomethylated. Each dot represents the methylation level of an individual DMR. Red and blue triangles contain the identified hypermethylated and hypomethylated DMRs, respectively. (*G*) Distribution of hypermethylated DMRs in KT premalignant cells among various genomic elements. GO analysis of all DEGs harboring hypermethylated DMRs in (*H*) promoter and enhancer or (*I*) gene body regions in KT premalignant cells. The number of genes in each category is indicated. Wnt-related categories are denoted in red.

antagonists were significantly enriched (*SI Appendix*, Fig. S11 *D* and *E*), including *Lrp4* and *Ctnnbip1* (Fig. 5*C*). Bisulfite Sanger sequencing confirmed the robustly decreased methylation levels in promoter regions of *Lrp4* and *Ctnnbip1* in Tet2CD-expressing KT cells (Fig. 5 *D* and *E*). Furthermore, 5hmC, the first-step oxidation product of 5mC, was detected in the same promoter regions of *Lrp4* and *Ctnnbip1* upon TET activity restoration (Fig. 5 *F* and *G*). Thus, TET-mediated oxidation of 5mC may trigger the DNA demethylation in the promoter regions of key Wnt-associated antagonizing genes, thus leading to the transcriptional augmentation of these anti-Wnt genes. Notably, analysis of TCGA LUAD datasets revealed that hypermethylation of the WNT antagonizing genes (e.g., *LRP4*, *CTNNBIP1*, *DACT1*, and *TMEM88*) correlated with their down-regulated expression in *TET*-mutant tumors when

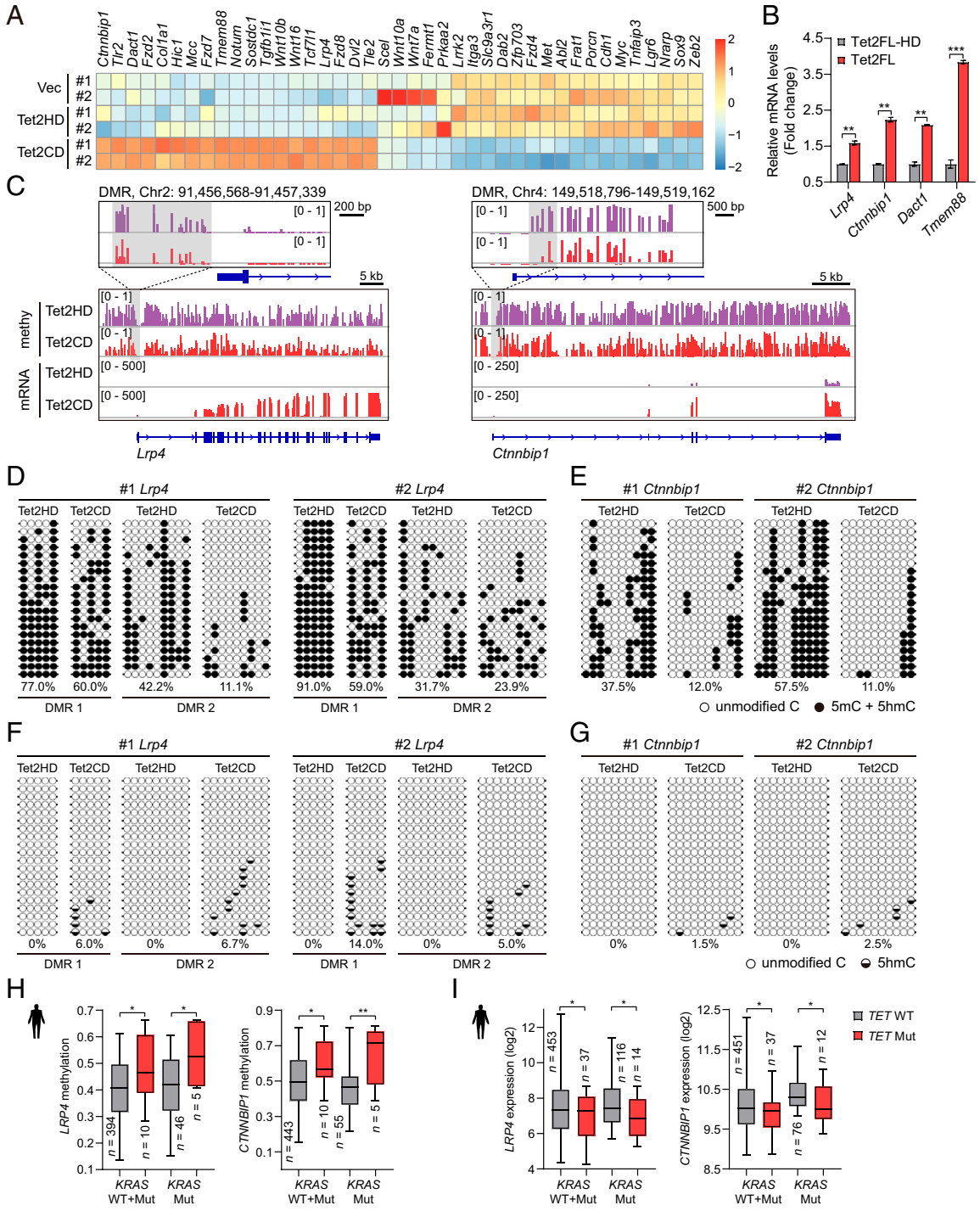

Fig. 5. TET-mediated demethylation induces transcriptional activation of Wnt antagonizing genes in KT cells. (*A*) Heat map showing relative expression levels of Wnt-associated DEGs in parental KT cells and KT cells complemented with Tet2CD (wild type) or Tet2HD (catalytically-inactive mutant). DEGs were defined as $\log_2$(fold change) ≥ 1 or ≤ -1 and adjusted *P* value ≤ 0.05. (*B*) qRT-PCR analysis of the Wnt antagonizing genes in KT cells complemented with the full-length mouse Tet2 (Tet2FL) or the catalytically-inactive mutant Tet2FL-HD. Data are presented as mean ± SEM. Statistical significance was calculated using two-tailed unpaired Student's *t* test. $^{**}P \leq 0.01$; $^{***}P \leq 0.001$. (*C*) Representative methylation (*Top*) and RNA-seq (*Bottom*) tracks of the Wnt antagonizing genes *Lrp4* (*Left*) and *Ctnnbip1* (*Right*) in KT cells complemented with Tet2CD or Tet2HD. Vertical bars of methylation tracks indicate the methylation level at individual CpG dyads. The gray-shaded area indicates the hypomethylated DMRs in the promoter regions of *Lrp4* and *Ctnnbip1* upon TET activity restoration. Methylation analysis of the (*D*) *Lrp4* or (*E*) *Ctnnbip1* promoter region in KT cells complemented with Tet2CD or Tet2HD by bisulfite Sanger sequencing. The open and black circles represent the unmethylated and methylated/hydroxymethylated CpG sites, respectively. APOBEC-coupled epigenetic (Sanger) sequencing (ACE-seq) analysis of the (*F*) *Lrp4* or (*G*) *Ctnnbip1* promoter region in KT cells complemented with Tet2CD or Tet2HD for the detection of 5hmC. The regions analyzed in *D*–*G* are indicated by the gray-shaded boxes in *C*. No. 1 and No. 2 are two independent KT cell lines. Differential (*H*) methylation or (*I*) expression levels of WNT antagonizing genes *LRP4* and *CTNNBIP1* in *TET*-mutant LUAD compared with *TET* wild-type LUAD. Source data of methylation values (β-values) were derived from TCGA Firehose Legacy (*H*), and source data of gene expression were derived from TCGA PanCancer Altas (*I*). In the box plots, whiskers indicate maxima and minima, box edges indicate 75th and 25th percentiles, and horizontal lines in the middle signify median. The number of samples is indicated for each group, and *P* values were calculated using a two-tailed unpaired Student's *t* test. $^{*}P \leq 0.05$; $^{**}P \leq 0.01$.

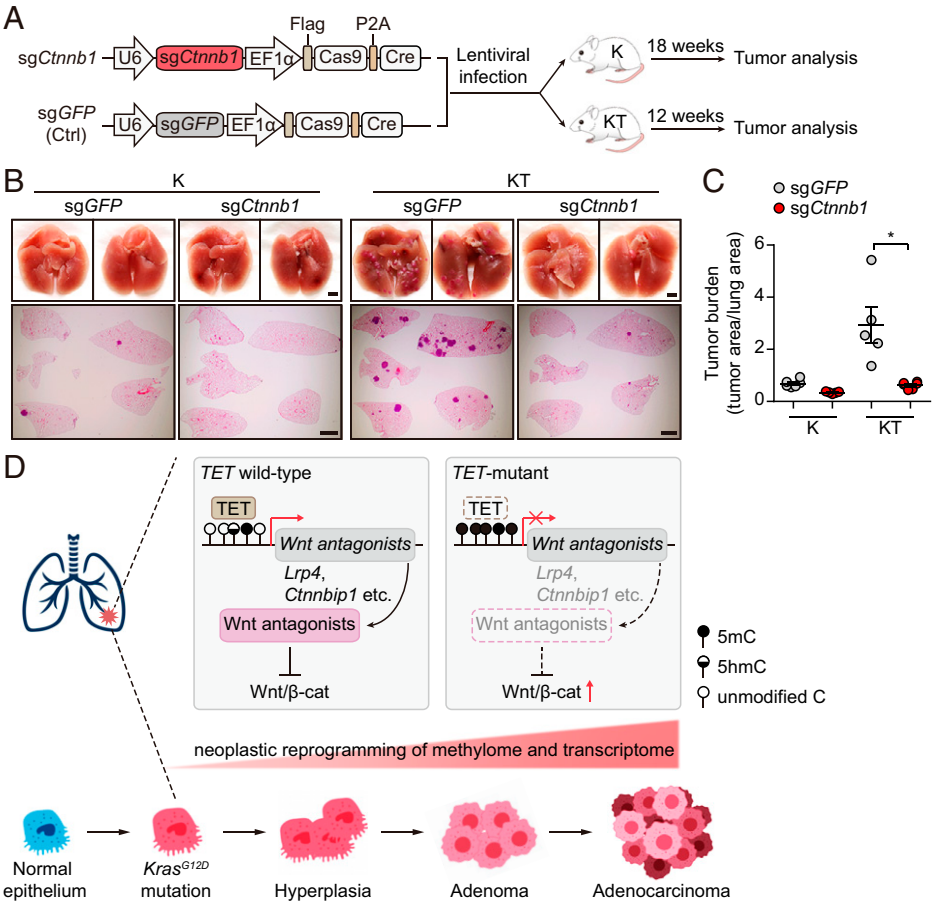

Fig. 6. Genetic depletion of β-catenin substantially reverts enhanced LUAD development in KT mice. (*A*) Schematic of lentiviral constructs expressing sgRNAs against *Ctnnb1* (*Catenin Beta 1*) or *GFP* together with Cas9 and Cre recombinase, which were used to induce lung tumorigenesis in K or KT mice. (*B*) Representative whole-mount views of tumor-bearing lung tissues and H&E-stained lung tumor sections from K (*Left*) or KT (*Right*) mice administered with the sg*GFP* or sg*Ctnnb1* lentiviruses. The tumor-bearing lung tissues were collected at 18 (*Left*) or 12 (*Right*) wk postinfection. (Scale bars, 2 mm.) (*C*) Corresponding quantification of tumor burden in K or KT mice infected with indicated lentiviruses. Each dot represents an individual mouse. For K mice, $n = 6$ for sg*GFP*-treated mice, and $n = 5$ for sg*Ctnnb1*-treated mice. For KT mice, $n = 5$ for sg*GFP*-treated mice, and $n = 6$ for sg*Ctnnb1*-treated mice. Data are presented as mean ± SEM. Statistical significance was assessed using two-tailed unpaired Student's *t* test with Welch's correction. $*P \leq 0.05$. (*D*) Working model illustrating the contribution of TET enzymes to antagonizing *Kras*-driven LUAD development. Lung epithelial cells can undergo neoplasia driven by $KRAS^{G12D}$ to initiate a premalignant, dysregulated growth. In general, $KRAS^{G12D}$ alone appears insufficient to drive LUAD development; however, combination with loss-of-function TET enables potent malignant transformation. In the *TET* wild-type setting, TET enzymes orchestrate dynamic balance of DNA methylation by their catalytic activity to maintain transcription of key Wnt-associated antagonizing targets, thus ensuring proper Wnt signaling and tumor suppression (*Left*). Impairment of TET-mediated oxidative DNA demethylation (for example, mutations or down-regulation of *TET* genes) reprograms the neoplastic landscapes of DNA methylome and transcriptome, increasing DNA methylation and silencing expression of Wnt antagonists, leading to hyperactivation of Wnt signaling and enhanced tumorigenic potential (*Right*).

compared with *TET* wild-type tumors (Fig. 5 *H* and *I* and *SI Appendix*, Fig. S11 *F* and *G*), particularly in the setting of mutant *KRAS*, supporting the relevance of our findings to human lung cancer. Altogether, these results identify the Wnt-associated antagonists as targets of TET-mediated oxidation and demonstrate how loss of dioxygenase activity can cause augmented Wnt signaling and enhanced tumorigenicity in KT LUAD cells.

Genetic Depletion of β-Catenin Impedes *Tet*-Deficient LUAD Progression. To investigate the contribution of imbalanced Wnt signaling pathway to lung tumorigenesis triggered by *Tet* deficiency in vivo, we employed a lentiviral-based pSECC (U6-sgRNA-EFS-Cas9-2A-Cre) system (54, 55) to genetically inhibit Wnt signaling activation through CRISPR/Cas9-mediated disruption of the *Ctnnb1* gene encoding β-catenin, which acts as an essential transcriptional effector in canonical Wnt signaling (56). For this purpose, we designed three sgRNAs targeting *Ctnnb1* (*SI Appendix*, Fig. S12*A*) and validated high-editing efficiency of these sgRNAs in the engineered 3T3 cells (*SI Appendix*, Fig. S12 *B*–*E*). K or KT mice were then administered via intranasal inhalation of the lentiviruses simultaneously expressing Cre, Cas9, and sgRNAs targeting either *Ctnnb1* or *GFP* control (Fig. 6*A*). Consequently, β-catenin depletion in KT mice led to a substantial decrease in overall tumor burden (Fig. 6 *B* and *C*). Of note, the extent of reversal of overall tumor burden in KT mice was much stronger than that in K mice (Fig. 6*C*). These data demonstrate that the enhanced tumorigenesis caused by *Tet* deficiency can be substantially reverted through the genetic inhibition of Wnt signaling.

Discussion

Mutations in epigenetic modifiers, as a characteristic of cancer cells, are thought to endow cells with selective plasticity to override normal differentiation and programmed growth control. The clear concurrence between mutations of *TET* family genes and *KRAS* and the poor survival of LUAD patients harboring these concurrent mutations have prompted us to consider

whether mouse models could be generated to recapitulate this clinical status and to study how TET dioxygenases control LUAD pathogenesis.

By using autochthonous GEMMs, we find that ablation of TET enzymes greatly accelerates $Kras^{G12D}$-driven LUAD development. We further demonstrate that the dioxygenase activity of TET enzymes is a prerequisite for anti-LUAD, suggesting an essential regulatory role of TET-mediated DNA oxidation in counterbalancing LUAD tumorigenicity. In early neoplastic lesions, TET loss induces a subtle increase in DNA methylation on a genome-wide scale and drives transcriptional reprogramming of premalignant lung epithelium, especially those Wnt-associated components (Fig. 6*D*). In malignant KT cells, the reintroduction of catalytically-active TET contributes to oxidative DNA demethylation at promoters of Wnt antagonizing genes (such as *Lrp4* and *Ctnnbip1*) and their up-regulated expression, indicating that the transcriptional reactivation of these antagonizing genes is dependent on TET catalytic activity (Fig. 6*D*). Inhibition of Wnt signaling via genetic depletion of *β-catenin* gene substantially mitigates aggressive LUAD development arising from *Tet* deficiency. The underappreciated relationship between TET loss and Wnt signaling activation thus highlights a vulnerability that might be therapeutically exploited for *TET* deficiency–induced lung neoplasms.

In previous mouse leukemia models (30, 31, 33), *Tet2* mutations alone can potentiate fitness of hematopoietic stem/progenitor cells to achieve clonal dominance, but acquisition of additional co-occurring genetic aberrations (e.g., $Flt3^{ITD}$, $Nras^{G12D}$, and $Rhoa^{G17V}$) is required to induce rapid leukemogenic transformation (57–59). Our study provides evidence for the mutational cooperativity between $Kras^{G12D}$ and *Tet* genes in the induction of mouse malignant LUAD, and the GEMMs generated here could recapitulate the phenotypic effects observed in LUAD patients. Unlike the phenotypic output in leukemiagenesis, in the absence of oncogenic mutant *Kras*, genetic deletion of *Tet* genes appears insufficient to drive lung tumor formation (*SI Appendix*, Fig. S5 *F* and *G*). This observation supports the notion that a combination with a critical oncogenic event is needed to facilitate neoplastic transformation for *Tet*-deficient lung epithelium. Furthermore, our data suggest that in the presence of oncogenic mutant *Kras*, *Tet* double and triple knockout mice develop more dramatic tumorigenic phenotypes than those single knockout mice (Fig. 2). Such dosage dependence among *Tet* family genes suggests that TET enzymes function collectively to prevent predisposing *Kras*-mutant cells from aggressive malignant transformation.

We have also shown that augmented Wnt signaling acts as a key factor to link TET loss to enhanced LUAD development (Fig. 6*D*). In established KT cell lines, antagonizing genes of Wnt signaling components, like *Lrp4* and *Ctnnbip1*, tend to acquire DNA hypermethylation on their promoters, thus reducing their expression. As a consequence, Wnt signaling is augmented, driving the malignant progression of LUAD. Consistent with our data, oncogenic *Kras* mutations alone are insufficient to endow lung epithelial cells with aggressive tumorigenic properties for rapid LUAD development, but augmented Wnt signaling can cooperate to accelerate lung tumorigenesis (60–64). Therapeutically, our findings provide a rationale for targeting Wnt signaling pathway as a therapeutic option in lung cancers harboring *TET* mutations, and point to epigenetic interventions to correct aberrant methylation as one modality for lung cancer treatment.

In summary, the *Tet* genes function as a critical tumor-suppressive role in autochthonous mouse models of LUAD. TET loss of function induces augmented Wnt signaling via transcriptional down-regulation of Wnt-associated antagonists due to DNA hypermethylation, thus contributing to aggressive LUAD development (Fig. 6*D*). Further studies will be necessary to explore targeting the Wnt signaling pathway to treat *TET*-deficient LUAD.

Materials and Methods

Mice. All animal experiments were performed under strict compliance with the Institutional Animal Care and Use Committee (IACUC) of Shanghai Institute of Biochemistry and Cell Biology (SIBCB), Chinese Academy of Sciences. All animals studies were performed according to protocols approved by the IACUC of SIBCB (Protocols: SIBCB-NAF-15-003-s202-013).

$Kras^{LSL\text{-}G12D/+}$ mice (45) (the Jackson Laboratory [JAX] stock no. 008179), $Rosa26^{LSL\text{-}tdTomato/+}$ mice (51) (JAX stock no. 007909), $Tet1^{flox/flox}$ mice (65), $Tet2^{flox/flox}$ mice (44, 66), $Tet3^{flox/flox}$ mice (67), and $Tet1^{flox/flox}$; $Tet2^{flox/flox}$; $Tet3^{flox/flox}$ mice (44) have been described previously. *Tet* conditional knockout mice were crossed with $Kras^{LSL\text{-}G12D/+}$ or $Rosa26^{LSL\text{-}tdTomato/+}$ mice to generate the mouse cohorts with desired genotypes used in this study. All mice were maintained on a mixed C57BL/6-129/Sv genetic background. Mice were housed in the specific pathogen-free animal facilities, kept at room temperature with a 12-h light/dark cycle in accordance with the guidelines and ethical regulations of the IACUC, and fed with regular chow and water by the facility staff.

Histology and Immunohistochemistry. The fixed tumor-bearing lung lobes were dehydrated in a graded ethanol series, embedded in paraffin, and cut into 5-μm sections. Adjacent sections were deparaffinized in xylene, rehydrated through an ethanol series into distilled water, and stained with hematoxylin and eosin (H&E) according to standard protocols.

For immunohistochemistry, paraffin-embedded sections were deparaffinized in xylene; rehydrated in 100, 95, 80, and 70% ethanol series into distilled water; subjected to antigen retrieval in a 10 mM sodium citrate buffer (pH 6.0) in a microwave for 15 min; and then incubated in 3% hydrogen peroxide for 15 min and washed three times in 0.2% phosphate-buffered saline with Tween 20 (PBST) (0.2% Tween 20 in PBS) at room temperature. The dried sections were blocked and permeabilized with 5 to 10% goat serum in PBST for at least 1 h. Sections were incubated with primary antibodies in appropriate antibody diluent at 4 °C overnight and washed three times in PBST, then incubated with biotin-conjugated secondary antibodies (anti-rabbit or anti-mouse IgG) by using Streptavidin HRP-Biotin DAB Detection Kit (Zsbio, SP-9000, SP-9001) as per the manufacturer's instructions followed by hematoxylin counterstaining. Primary antibodies to the following were used: Ki-67 (Cell Signaling, no. 12202, 1:200), SPC (Millipore, no. ABC99, 1:200), NKX2-1 (Abcam, ab133638, 1:250), and SCGB1A1 (Seven Hills, WRAB-3950, 1:10,000).

For 5mC and 5hmC immunostaining, before being incubated with block solution, sections were treated with 4N HCl solution (diluted in distilled water) for 15 min and then neutralized with 100 mM Tris-HCl (pH 8.5) for 10 min and rinsed in PBST, followed by incubation with primary anti-5hmC (Eurogentec, BI-MECY-0100, 1:1,000) and anti-5hmC (Active Motif, no. 39792, 1:2,000) antibodies at 4 °C overnight.

Histological slides were scanned with a Zeiss Axio Zoom V16 stereoscope, and photomicrographs were captured on an Olympus BX51 microscope.

Cloning of *Tet2* Lentiviral Constructs. The truncated wild-type mouse *Tet2* cDNA containing the catalytic domain (from 3,124 to 5,739 bp of full-length mouse *Tet2* coding sequences, NCBI NM_001040400.2) (*Tet2*CD) or the full-length wild-type mouse *Tet2* cDNA (NCBI NM_001040400.2, 5,739 bp) (*Tet2*FL) was obtained from pcDNA3-FLAG-*Tet2*CD or pCAG-*Tet2*FL, digested with *Eco*RI and *Not*I, purified with QIAquick Gel Extraction Kit (Qiagen), and then subcloned into pCDH-CMV-3×FLAG-EF1α-Cre and pCDH-CMV-3×FLAG-EF1α-copGFP vectors (68). The catalytically-inactive mutants with disrupted iron-binding site (amino acid substitutions from $H_{1295}R_{1296}D_{1297}$ to $Y_{1295}R_{1296}A_{1297}$) (*Tet2*HD or *Tet2*FL-HD) were obtained from pcDNA3-FLAG-*Tet2*HD or pCAG-*Tet2*FL-HD and constructed in the same vectors. All constructs were confirmed by Sanger sequencing.

Lentiviral CRISPR-Mediated Gene Perturbation. The pSECC lentiviral vector (Addgene, no. 60820) and cloning strategy were previously described (54). In brief, three sgRNAs targeting *Ctnnb1* were designed using Optimized CRISPR Design, and sg*GFP* was previously reported (69). sgRNA sequences to the following were used: sg*Ctnnb1*.1, 5′-CTGTGGTGGTGGCACCAGAA-3′; sg*Ctnnb1*.2, 5′-AGCTCCTTCCCTGAGTGGCA-3′; sg*Ctnnb1*.3, 5′-AGCTACTTGCTCTTGCGTGA-3′; and sg*GFP*, 5′-GGGCGAGGAGCTGTTCACCG-3′. For sgRNA cloning, pSECC vector was digested with *Bsm*BI and ligated with *Bsm*BI-compatible annealed oligonucleotides of sgRNAs. pSECC lentiviruses were produced as described in the *SI Appendix, Materials and Methods*.

GENETICS

To evaluate sgRNA efficiency, 3T3 reporter cells were infected with pSECC lentiviruses expressing the respective sgRNAs, and then GFP^+ cells were sorted by FACS to enrich for pSECC-containing cells at least 72 h after infection. The regions of *Ctnnb1* targeted by the respective sgRNAs were PCR amplified from genomic DNA of GFP^+ cells, then PCR products were cloned using pClone007 Versatile Simple Vector Kit (TSINGKE, 007VSm) and analyzed by massively parallel Sanger sequencing. Genotyping primers for sgRNA-targeting region of *Ctnnb1* are as follows: *Ctnnb1*-F, 5′-GCCAGACTGCCTTTGTTCTC-3′; and *Ctnnb1*-R, 5′-TGTGGCTGAGCTGTCACACA-3′.

pSECC lentiviruses expressing the respective highly-efficient *Ctnnb1* sgRNAs were pooled together at a ratio of 1:1:1 and then were delivered into mice via intranasal inhalation with appropriate transforming units (TFUs) per mouse.

Isolation of Primary Lung and LUAD Cells. Mice with lesions or LUAD tumors were euthanized at 3 or 12 to 16 wk after adenoviral infection. For early-stage analysis, all samples were harvested by dissociating entire lungs bearing hyperplasia. Following euthanasia, dissected lungs were iced, minced, and incubated in 5 mL protease and DNase solution (Collagenase Type I [300 U/mL, Gibco, 17100017], DNase I [100 μg/mL, Roche, 10104159001] in Dulbecco's modified Eagle medium (DMEM) [Gibco, 11965-118] or Roswell Park Memorial Institute (RPMI) 1640 [Gibco, 11875-119] supplemented with 10% heat-inactivated fetal bovine serum (FBS) [Gibco] and 5% penicillin/streptomycin [Gibco, 15140-122]) at 37 °C for 45 min with frequent rotation (70, 71). Dissociated cells were then filtered through a 100-μm cell strainer (Falcon, 352350) and centrifuged at 300 × *g* for 5 min at room temperature. The supernatant was removed by aspiration, and cells were resuspended in red blood cell lysis buffer (3 to 5 mL, Beyotime, C3702) for 3 min. Cells were then washed with FACS buffer (2% FBS in Dulbecco's phosphate-buffered saline [DPBS], supplemented with 5% pen-strep) and centrifuged at 300 × *g* for 3 min at room temperature. The supernatant was removed, and the pellet was resuspended in FACS buffer before being passed through a 40-μm cell strainer (Falcon, 352340) and counted for use in FACS (see *FACS*). For large LUAD tumors at 12 to 16 wk, they were microdissected from tumor-bearing lung tissues and then processed similarly to the procedures for early-stage entire lungs.

FACS. Cells were prepared as above (see *Isolation of Primary Lung and LUAD Cells*) at 1×10^6/100 μL and then were stained for 20 min on ice with the antibodies anti-CD45 APC (BioLegend, no. 103112, 1:100), anti-CD31 APC (BioLegend, no. 102510, 1:100), and anti-CD326 (EPCAM) APC/Cy7 (BioLegend, no. 118218, 1:100) and washed three times with FACS buffer. Three-minute, 300 × *g* spins at room temperature were performed in between washes to pellet the cells. DAPI as a viability dye (BD Bioscience, no. 564907) was added to each sample to identify dead cells before FACS sorting. Single stain controls and fluorophore minus one controls were included for each experiment. FACS sorting of stained primary cells was performed using a BD FACSAria Special Order Research Product (SORP), and analysis was done with FlowJo (v10.0.7). To isolate premalignant cells, dissociated lung cells were stained and sorted for $DAPI^-$/$CD45^-$/$CD31^-$/$tdTomato^+$/$EPCAM^+$ live cells (70–73). To isolate primary LUAD cells from KT tumors, total cancer cell fraction was gated as $DAPI^-$/$CD45^-$/$CD31^-$/$tdTomato^+$ live cells (61, 72, 73).

RNA and DNA Isolation. Total RNA and DNA were simultaneously isolated with AllPrep DNA/RNA Micro Kit (Qiagen, 80284) or Mini Kit (Qiagen, 0204). Isolated RNA and DNA were subjected to RNA-seq and PBAT WGBS, respectively.

RNA-seq Library Preparation. For premalignant cells, lung tissues with hyperplasia were dissociated at 3 wk after adenoviral infection, and cells were stained and sorted as described above (see *FACS*).

Approximately 500 premalignant cells were lysed, and the reverse-transcribed RNA was preamplified to obtain enough cDNA by a modified SMART-Seq2 protocol (74). cDNA was quantified by Qubit 4 (Invitrogen), and then 1 ng cDNA was used for DNA library construction with TruePrep DNA Library Prep Kit V2 for Illumina (Vazyme, TD503).

For KT LUAD cells, DNA library construction was performed with about 1 μg of extracted RNA using VAHTS mRNA-seq V3 Library Prep Kit for Illumina (Vazyme, NR611) following the manual.

RNA-seq Data Analysis. First, the raw pair-end RNA-seq FASTQ (a format file that is mostly used to store short-read data from high-throughput sequencing) data were trimmed to remove low-quality bases and adaptor sequences by Trim Galore (v0.5.0) with default settings. Then, the clean RNA-seq FASTQ data were mapped to mouse reference genome mm10 using Hisat2 (v2.1.0) with default parameters. DEG analysis was performed by using DESeq2 package with the raw count. Only genes with adjusted *P* value less than 0.05 and at least twofold change were considered to be differentially expressed. DEGs were submitted to the Database for Annotation, Visualization and Integrated Discovery (DAVID) 6.7 (https://david.ncifcrf.gov) for Gene Ontology (GO) and Kyoto Encyclopedia of Genes and Genomes (KEGG) pathway enrichment analyses.

PBAT Library Preparation. About 1 ng of isolated genomic DNA was used for PBAT library construction using a slightly modified protocol as previously reported (75). Briefly, genomic DNA spiked with 1% unmethylated lambda DNA (Thermo) was converted by bisulfite and purified with EZ DNA Methylation-Direct Kit (Zymo Research, D5021). Then, random nonamer primers with a 5′ biotin tag and a truncated Illumina P5 adaptor and 50 U Klenow polymerase (NEB) were used to amplify the bisulfite-converted templates linearly. The excess primers were removed using 40 U Exonuclease I (NEB) before amplified, and products were purified with 0.8× Agencourt AmpureXP beads (Beckman Coulter). The newly synthesized DNA strands with biotin were captured with Dynabeads M280 Streptavidin (Invitrogen), and the original bisulfite-treated DNA templates were washed away by 0.1 N NaOH. The second strands were synthesized using 50 U Klenow polymerase with random nonamer primers containing a truncated P7 Illumina adaptor. The beads with double-strand DNA products were further collected and washed several times, and the libraries were generated by PCR amplification using 2x KAPA HiFi HotStart ReadyMix (KAPA Biosystems), together with 0.4 μM Illumina Forward primer and 0.4 μM preindexed Illumina Reverse primer. Amplified libraries were purified with 0.8× Agencourt Ampure XPbeads twice and then assessed with Agilent 2100 and quantified with a standard curve-based qPCR assay. The final quality-ensured libraries were pooled and sequenced on the Illumina HiSeq X Ten sequencer for 150 bp paired-end sequencing.

PBAT Data Analysis. By using Trim Galore (v0.5.0), raw pair-end FASTQ reads were trimmed to remove low-quality bases and adaptor sequences. The remaining clean reads were mapped to mouse reference genome mm10 with single-end and nondirectional mapping parameters by using BS-Seeker2 (v2.1.8) (76). Duplicated reads were removed using SAMtools (v1.4) for the subsequent analysis. Bisulfite conversion rate was estimated by the lambda genome, which was built as the extra chromosome. Only samples with at least 98.5% bisulfite conversion rate were kept for DNA methylation analysis.

CGmapTools (v0.1.2) (77) was used for DNA methylation downstream analysis following BS-Seeker2. The single-C files of the replicates were merged together, and only the single CpG sites with at least 3× coverage were kept for further analysis. DMRs were filtered by the length (maximal distance between two adjacent cytosines is less than 100 bp, and DMR length is less than 1,000 bp), CpG number (at least five CpG sites), and methylation level difference between K and KT samples (at least 20% absolute methylation level difference).

The annotated information of exon, intron, intergenic, and CGI (CpG island) was downloaded from the University of California Santa Cruz (UCSC) Genome Browser (mm10), and all repetitive elements were annotated by using RepeatMasker (mm10). Center regions of H3K4me1 and H3K27ac ChIP-seq peaks in $Kras^{G12D}$ lung tumors were defined as typical active enhancers (78). Promoters were defined as the regions from − 0.5 to + 1.5 kb of the transcription start site.

For integrated analysis of RNA-seq and whole-genome DNA methylation data, we first annotated the genes containing hypermethylated DMRs in promoter, enhancer, and intron regions. Then, DEGs were intersected with these genes containing hypermethylated DMRs to obtain commonly changed genes. The commonly changed genes were submitted to DAVID 6.7 for GO analysis.

TAPS Analysis. Whole-genome TAPS libraries were constructed as previously described (53). In brief, 100 ng genomic DNA spiked with 1.0% of fully CpG-methylated lambda DNA was sonicated in EB buffer and purified by DNA clean beads to select for the desired DNA fragment size. DNA fragments were oxidized by recombinant human TET2CD twice and then reduced with pyridine borane. The library was amplified with KAPA HiFi HotStart Uracil+ ReadyMix PCR Kit (KAPA Biosystems).

For data analysis, the raw data were trimmed by Trim Galore (v0.5.0) with default settings. Then, the clean data were mapped to mm10 using bwa (0.7.15). Duplicated reads were removed using Picard (2.21.2). Methylation levels were called using astair call (3.2.6). CGmapTools (v0.1.2) was used for DNA methylation downstream analysis. Only samples with at least 95.5% TAPS conversion rate were kept for DNA methylation analysis.

ACE Sanger Sequencing. ACE Sanger sequencing was performed following the published protocol as previously described (79). In brief, 50 ng genomic DNA spiked with 5% of fully CpG-methylated lambda DNA and hydroxymethylated T4 genomic DNA (T4-hmC) was glucosylated using UDPglucose and T4 β-glucosyltransferase (βGT) at 37 °C for 1 h. Then, 1 μL of dimethyl sulphoxide (DMSO) was added to terminate the reaction, and the sample was denatured at 95 °C for 5 min and snap cooled by transfer to a PCR tube rack preincubated

at − 80 °C. Before thawing, reaction buffer was overlaid to a final concentration of 20 mM MES pH 6.0 + 0.1% Tween, and recombinant human APOBEC3A was added to a final concentration of 5 μM in a total volume of 10 μL. The deamination reactions were incubated under linear ramping temperature conditions from 4 to 50 °C over 2 h. Then, PCR primers were designed to amplify the target genomic regions and detect 5hmC levels with Sanger sequencing.

Statistics and Reproducibility. Statistical analyses were performing using GraphPad Prism v.8.4.2 (GraphPad Software). All data are represented as mean ± SEM of individual data points from at least two independent biological replicates. Two-tailed unpaired Student's *t* test, χ^2 test, log-rank (Mantel–Cox) test, and one-sided Fisher's exact test were used to determine statistical significance. In all types of statistical analysis, values of $P \leq 0.05$ were considered significant. *N* values and statistical method used in each experiment are indicated in the figure legends or in the figures themselves. No statistical method was used to predetermine sample size. No method of randomization was used. The investigators were not blinded to allocation during experiments or outcome assessment.

All other details of materials and methods are included in *SI Appendix, Materials and Methods*.

Data Availability. All sequencing data, including RNA-seq, WGBS, and TAPS data, reported in this study have been deposited in the Gene Expression Omnibus database (accession no. GSE185615). All other relevant data that support the findings of this study are included in the article and/or *SI Appendix*.

ACKNOWLEDGMENTS. We thank L.-A. Xu and C.-H. Wang for assistance with quantitative mass spectrometry analysis and H.-Q. Dai, X.-K. Han, and J. Zhang for technical help. We also thank X. Sun, Y.-J. Shi, S.-Y. Sun, J. Huang, X.-Q. Kong, L.-L. Shen, and G.-N. Liang for insightful comments. This work was supported by the National Key Research and Development Program of China (Grant 2017YFA0102701 to G.-L.X., Grant 2017YFA0505501 to H.J., and Grant 2020YFA0803300 to H.J.), the National Natural Science Foundation of China (Grants 31830018 and 31430049 to G.-L.X. and Grants 31621003, 81872312, 82030083, and 82011540007 to H.J.), the Strategic Priority Research Program of the Chinese Academy of Sciences (Grant XDB19010102 to G.-L.X. and Grant XDB19020201 to H.J.), the Basic Frontier Scientific Research Program of the Chinese Academy of Sciences (Grant ZDBS-LY-SM006 to H.J.), the International Cooperation Project of Chinese Academy of Sciences (Grant 153D31KYSB20190035 to H.J.), and the Newton International Exchange Award (IE160973 to G.-L.X. and C.P.W.).

1. L. A. Torre *et al.*, Global cancer statistics, 2012. *CA Cancer J. Clin.* **65**, 87–108 (2015).
2. C. Gridelli *et al.*, Non-small-cell lung cancer. *Nat. Rev. Dis. Primers* **1**, 15009 (2015).
3. Cancer Genome Atlas Research Network, Comprehensive molecular profiling of lung adenocarcinoma. *Nature* **511**, 543–550 (2014).
4. J. D. Campbell *et al.*; Cancer Genome Atlas Research Network, Distinct patterns of somatic genome alterations in lung adenocarcinomas and squamous cell carcinomas. *Nat. Genet.* **48**, 607–616 (2016).
5. H. Ji *et al.*, LKB1 modulates lung cancer differentiation and metastasis. *Nature* **448**, 807–810 (2007).
6. T. J. Lynch *et al.*, Activating mutations in the epidermal growth factor receptor underlying responsiveness of non-small-cell lung cancer to gefitinib. *N. Engl. J. Med.* **350**, 2129–2139 (2004).
7. E. L. Kwak *et al.*, Anaplastic lymphoma kinase inhibition in non-small-cell lung cancer. *N. Engl. J. Med.* **363**, 1693–1703 (2010).
8. A. T. Shaw, B. J. Solomon, Crizotinib in ROS1-rearranged non-small-cell lung cancer. *N. Engl. J. Med.* **372**, 683–684 (2015).
9. D. M. Hyman *et al.*, Vemurafenib in multiple nonmelanoma cancers with BRAF V600 mutations. *N. Engl. J. Med.* **373**, 726–736 (2015).
10. H. Borghaei *et al.*, Nivolumab versus docetaxel in advanced nonsquamous non-small-cell lung cancer. *N. Engl. J. Med.* **373**, 1627–1639 (2015).
11. M. Reck *et al.*; KEYNOTE-024 Investigators, Pembrolizumab versus chemotherapy for PD-L1-positive non-small-cell lung cancer. *N. Engl. J. Med.* **375**, 1823–1833 (2016).
12. R. S. Herbst, D. Morgensztern, C. Boshoff, The biology and management of non-small cell lung cancer. *Nature* **553**, 446–454 (2018).
13. D. Hanahan, R. A. Weinberg, Hallmarks of cancer: The next generation. *Cell* **144**, 646–674 (2011).
14. C. D. Allis, T. Jenuwein, The molecular hallmarks of epigenetic control. *Nat. Rev. Genet.* **17**, 487–500 (2016).
15. W. A. Flavahan, E. Gaskell, B. E. Bernstein, Epigenetic plasticity and the hallmarks of cancer. *Science* **357**, eaal2380 (2017).
16. H. P. Mohammad, O. Barbash, C. L. Creasy, Targeting epigenetic modifications in cancer therapy: Erasing the roadmap to cancer. *Nat. Med.* **25**, 403–418 (2019).
17. S. E. Bates, Epigenetic therapies for cancer. *N. Engl. J. Med.* **383**, 650–663 (2020).
18. M. Guillamot, L. Cimmino, I. Aifantis, The impact of DNA methylation in hematopoietic malignancies. *Trends Cancer* **2**, 70–83 (2016).
19. M. Esteller, Epigenetics in cancer. *N. Engl. J. Med.* **358**, 1148–1159 (2008).
20. M. Tahiliani *et al.*, Conversion of 5-methylcytosine to 5-hydroxymethylcytosine in mammalian DNA by MLL partner TET1. *Science* **324**, 930–935 (2009).
21. S. Ito *et al.*, Tet proteins can convert 5-methylcytosine to 5-formylcytosine and 5-carboxylcytosine. *Science* **333**, 1300–1303 (2011).
22. Y. F. He *et al.*, Tet-mediated formation of 5-carboxylcytosine and its excision by TDG in mammalian DNA. *Science* **333**, 1303–1307 (2011).
23. G. L. Xu, M. Bochtler, Reversal of nucleobase methylation by dioxygenases. *Nat. Chem. Biol.* **16**, 1160–1169 (2020).
24. X. Wu, Y. Zhang, TET-mediated active DNA demethylation: Mechanism, function and beyond. *Nat. Rev. Genet.* **18**, 517–534 (2017).
25. O. Abdel-Wahab *et al.*, Genetic characterization of TET1, TET2, and TET3 alterations in myeloid malignancies. *Blood* **114**, 144–147 (2009).
26. F. Delhommeau *et al.*, Mutation in TET2 in myeloid cancers. *N. Engl. J. Med.* **360**, 2289–2301 (2009).
27. S. M. Langemeijer *et al.*, Acquired mutations in TET2 are common in myelodysplastic syndromes. *Nat. Genet.* **41**, 838–842 (2009).
28. R. L. Bowman, R. L. Levine, TET2 in normal and malignant hematopoiesis. *Cold Spring Harb. Perspect. Med.* **7**, a026518 (2017).
29. M. Ko *et al.*, Impaired hydroxylation of 5-methylcytosine in myeloid cancers with mutant TET2. *Nature* **468**, 839–843 (2010).
30. K. Moran-Crusio *et al.*, Tet2 loss leads to increased hematopoietic stem cell self-renewal and myeloid transformation. *Cancer Cell* **20**, 11–24 (2011).
31. C. Quivoron *et al.*, TET2 inactivation results in pleiotropic hematopoietic abnormalities in mouse and is a recurrent event during human lymphomagenesis. *Cancer Cell* **20**, 25–38 (2011).
32. L. Cimmino *et al.*, TET1 is a tumor suppressor of hematopoietic malignancy. *Nat. Immunol.* **16**, 653–662 (2015).
33. J. An *et al.*, Acute loss of TET function results in aggressive myeloid cancer in mice. *Nat. Commun.* **6**, 10071 (2015).
34. Y. Huang, A. Rao, Connections between TET proteins and aberrant DNA modification in cancer. *Trends Genet.* **30**, 464–474 (2014).
35. K. D. Rasmussen, K. Helin, Role of TET enzymes in DNA methylation, development, and cancer. *Genes Dev.* **30**, 733–750 (2016).
36. J. K. Bray, M. M. Dawlaty, A. Verma, A. Maitra, Roles and regulations of TET enzymes in solid tumors. *Trends Cancer* **7**, 635–646 (2021).
37. L. Ding *et al.*, Somatic mutations affect key pathways in lung adenocarcinoma. *Nature* **455**, 1069–1075 (2008).
38. M. Imielinski *et al.*, Mapping the hallmarks of lung adenocarcinoma with massively parallel sequencing. *Cell* **150**, 1107–1120 (2012).
39. N. A. Rizvi *et al.*, Cancer immunology. Mutational landscape determines sensitivity to PD-1 blockade in non-small cell lung cancer. *Science* **348**, 124–128 (2015).
40. E. J. Jordan *et al.*, Prospective comprehensive molecular characterization of lung adenocarcinomas for efficient patient matching to approved and emerging therapies. *Cancer Discov.* **7**, 596–609 (2017).
41. Y. Sato *et al.*, Integrated molecular analysis of clear-cell renal cell carcinoma. *Nat. Genet.* **45**, 860–867 (2013).
42. S. Seshagiri *et al.*, Recurrent R-spondin fusions in colon cancer. *Nature* **488**, 660–664 (2012).
43. M. L. Nickerson *et al.*, Somatic alterations contributing to metastasis of a castration-resistant prostate cancer. *Hum. Mutat.* **34**, 1231–1241 (2013).
44. H. Q. Dai *et al.*, TET-mediated DNA demethylation controls gastrulation by regulating Lefty-Nodal signalling. *Nature* **538**, 528–532 (2016).
45. E. L. Jackson *et al.*, Analysis of lung tumor initiation and progression using conditional expression of oncogenic K-ras. *Genes Dev.* **15**, 3243–3248 (2001).
46. M. DuPage, A. L. Dooley, T. Jacks, Conditional mouse lung cancer models using adenoviral or lentiviral delivery of Cre recombinase. *Nat. Protoc.* **4**, 1064–1072 (2009).
47. X. Xu *et al.*, Evidence for type II cells as cells of origin of K-Ras-induced distal lung adenocarcinoma. *Proc. Natl. Acad. Sci. U.S.A.* **109**, 4910–4915 (2012).
48. S. Mainardi *et al.*, Identification of cancer initiating cells in K-Ras driven lung adenocarcinoma. *Proc. Natl. Acad. Sci. U.S.A.* **111**, 255–260 (2014).
49. K. D. Sutherland *et al.*, Multiple cells-of-origin of mutant K-Ras-induced mouse lung adenocarcinoma. *Proc. Natl. Acad. Sci. U.S.A.* **111**, 4952–4957 (2014).
50. M. M. Winslow *et al.*, Suppression of lung adenocarcinoma progression by Nkx2-1. *Nature* **473**, 101–104 (2011).
51. L. Madisen *et al.*, A robust and high-throughput Cre reporting and characterization system for the whole mouse brain. *Nat. Neurosci.* **13**, 133–140 (2010).
52. D. A. Tuveson *et al.*, Endogenous oncogenic K-ras(G12D) stimulates proliferation and widespread neoplastic and developmental defects. *Cancer Cell* **5**, 375–387 (2004).
53. Y. Liu *et al.*, Bisulfite-free direct detection of 5-methylcytosine and 5-hydroxy methylcytosine at base resolution. *Nat. Biotechnol.* **37**, 424–429 (2019).
54. F. J. Sánchez-Rivera *et al.*, Rapid modelling of cooperating genetic events in cancer through somatic genome editing. *Nature* **516**, 428–431 (2014).
55. Q. Wu *et al.*, In vivo CRISPR screening unveils histone demethylase UTX as an important epigenetic regulator in lung tumorigenesis. *Proc. Natl. Acad. Sci. U.S.A.* **115**, E3978–E3986 (2018).
56. J. M. Bugter, N. Fenderico, M. M. Maurice, Mutations and mechanisms of WNT pathway tumour suppressors in cancer. *Nat. Rev. Cancer* **21**, 5–21 (2021).
57. A. H. Shih *et al.*, Mutational cooperativity linked to combinatorial epigenetic gain of function in acute myeloid leukemia. *Cancer Cell* **27**, 502–515 (2015).

58. H. Kunimoto *et al.*, Cooperative epigenetic remodeling by TET2 loss and NRAS mutation drives myeloid transformation and MEK inhibitor sensitivity. *Cancer Cell* **33**, 44–59.e8 (2018).
59. J. R. Cortes *et al.*, RHOA G17V induces T follicular helper cell specification and promotes lymphomagenesis. *Cancer Cell* **33**, 259–273.e7 (2018).
60. E. C. Pacheco-Pinedo *et al.*, Wnt/β-catenin signaling accelerates mouse lung tumorigenesis by imposing an embryonic distal progenitor phenotype on lung epithelium. *J. Clin. Invest.* **121**, 1935–1945 (2011).
61. T. Tammela *et al.*, A Wnt-producing niche drives proliferative potential and progression in lung adenocarcinoma. *Nature* **545**, 355–359 (2017).
62. M. Vaz *et al.*, Chronic cigarette smoke-induced epigenomic changes precede sensitization of bronchial epithelial cells to single-step transformation by KRAS mutations. *Cancer Cell* **32**, 360–376.e6 (2017).
63. A. N. Nabhan, D. G. Brownfield, P. B. Harbury, M. A. Krasnow, T. J. Desai, Single-cell Wnt signaling niches maintain stemness of alveolar type 2 cells. *Science* **359**, 1118–1123 (2018).
64. W. J. Zacharias *et al.*, Regeneration of the lung alveolus by an evolutionarily conserved epithelial progenitor. *Nature* **555**, 251–255 (2018).
65. R. R. Zhang *et al.*, Tet1 regulates adult hippocampal neurogenesis and cognition. *Cell Stem Cell* **13**, 237–245 (2013).
66. X. Hu *et al.*, Tet and TDG mediate DNA demethylation essential for mesenchymal-to-epithelial transition in somatic cell reprogramming. *Cell Stem Cell* **14**, 512–522 (2014).
67. T. P. Gu *et al.*, The role of Tet3 DNA dioxygenase in epigenetic reprogramming by oocytes. *Nature* **477**, 606–610 (2011).
68. X. Han *et al.*, Transdifferentiation of lung adenocarcinoma in mice with Lkb1 deficiency to squamous cell carcinoma. *Nat. Commun.* **5**, 3261 (2014).
69. W. Xue *et al.*, CRISPR-mediated direct mutation of cancer genes in the mouse liver. *Nature* **514**, 380–384 (2014).
70. Q. Liu *et al.*, Lung regeneration by multipotent stem cells residing at the bronchioalveolar-duct junction. *Nat. Genet.* **51**, 728–738 (2019).
71. A. F. M. Dost *et al.*, Organoids model transcriptional hallmarks of oncogenic KRAS activation in lung epithelial progenitor cells. *Cell Stem Cell* **27**, 663–678 (2020).
72. N. D. Marjanovic *et al.*, Emergence of a high-plasticity cell state during lung cancer evolution. *Cancer Cell* **38**, 229–246.e13 (2020).
73. L. M. LaFave *et al.*, Epigenomic state transitions characterize tumor progression in mouse lung adenocarcinoma. *Cancer Cell* **38**, 212–228 (2020).
74. S. Picelli *et al.*, Smart-seq2 for sensitive full-length transcriptome profiling in single cells. *Nat. Methods* **10**, 1096–1098 (2013).
75. S. A. Smallwood *et al.*, Single-cell genome-wide bisulfite sequencing for assessing epigenetic heterogeneity. *Nat. Methods* **11**, 817–820 (2014).
76. W. Guo *et al.*, BS-Seeker2: A versatile aligning pipeline for bisulfite sequencing data. *BMC Genomics* **14**, 774 (2013).
77. W. Guo *et al.*, CGmapTools improves the precision of heterozygous SNV calls and supports allele-specific methylation detection and visualization in bisulfite-sequencing data. *Bioinformatics* **34**, 381–387 (2018).
78. H. Alam *et al.*, KMT2D deficiency impairs super-enhancers to confer a glycolytic vulnerability in lung cancer. *Cancer Cell* **37**, 599–617 (2020).
79. E. K. Schutsky *et al.*, Nondestructive, base-resolution sequencing of 5-hydroxymethylcytosine using a DNA deaminase. *Nat. Biotechnol.* 10.1038/nbt.4204. (2018).